JOURNAL OF AIRCRAFT
Vol. 30, No. 5, Sept.–Oct. 1993

Euler Analysis of Forebody-Strake Vortex Flows at Supersonic Speeds

O. J. Rose*
Lockheed Engineering and Sciences Company, Hampton, Virginia 23666
and
James L. Pittman†
NASA Langley Research Center, Hampton, Virginia 23665

This article discusses the flowfield, surface pressure, and integrated forces and moments obtained by solving the Euler equations numerically for a fighter-type forebody with uncambered sharp leading-edge strakes. Predictions are compared with experiment for freestream Mach numbers 1.6, 1.8, and 2.0, and angles of attack from approximately 0–14 deg. Comparison with experimental data showed that the Euler method correctly predicted the leading-edge vortices and embedded shocks which arise at higher angles of attack. However, the vortices due to embedded shock-induced separation, which occurred on the upper forebody aft of the canopy, were not predicted. The effects of crossflow grid density, artificial viscosity, angle of attack, and streamwise station on the computed-flow characteristics were examined. It was found that increasing crossflow grid density resulted in a better resolution of the flowfield details, but the general characteristics of the flowfield remained the same, provided a threshold of approximately 3000 crossflow grid cells was exceeded. The flow solutions were also found to be relatively insensitive to variations in artificial viscosity. The predicted strength of leading-edge vortices generally increased with increasing angle of attack, streamwise station, and Mach number.

Nomenclature

$A.V.$	=	second-order artificial viscosity constant
C_D	=	drag coefficient
C_L	=	lift coefficient
C_m	=	pitching moment coefficient
C_p	=	pressure coefficient
E	=	total internal energy, Eq. (3)
f, g, h	=	defined by Eqs. (2b–d)
$\bar{f}, \bar{g}, \bar{h}$	=	defined by Eqs. (8b–d)
H	=	total enthalpy, Eq. (4)
$\bar{I}$	=	defined by Eq. (8e)
M	=	freestream Mach number
p	=	static pressure
p_t	=	total pressure
$\boldsymbol{Q}$	=	flux vector, Eq. (2a)
R	=	radial direction in spherical coordinates, Fig. 2 (also gas constant for ideal gas)
u, v, w	=	Cartesian velocity components
$\bar{u}, \bar{v}, \bar{w}$	=	transformed velocity components, Eq. (6)
x_{LE}	=	spanwise position of leading edge
$\bar{x}, \bar{y}$	=	spherical coordinates, Eqs. (5a) and (5b)
x, y, z	=	Cartesian coordinate system; origin at configuration apex, Fig. 2
α	=	angle of attack, deg
γ	=	ratio of specific heats
η	=	fraction of local configuration semispan, x/x_{LE}
ρ	=	density

Introduction

FLIGHT vehicles are usually designed for attached flow at cruise conditions. However, many flight vehicles also operate at high angles of attack where vortex-dominated flows are common. These flows have been extensively investigated, since vortex flow can significantly influence the performance, stability, and control of a vehicle. Numerous articles on the subject have been published in recent years.[1–12]

One particular configuration of interest for tactical aircraft is the fuselage-strake-wing combination that is used by several current-generation fighter aircraft. The strake creates a powerful vortex at high angle of attack that enhances maneuverability. The increasing importance of supersonic flight as a means of improving aircraft survivability stimulated the development of a method for strake design using a full-potential method under typical supersonic cruise conditions.[13] This strake-design technique was validated experimentally on a forebody-strake configuration at low angles of attack as presented in Ref. 13.

The objective of the present investigation is to computationally study the leading-edge vortex formation on an uncambered strake with sharp leading edges for typical supersonic-maneuver conditions. Several investigators have examined the ability of Euler solvers to predict leading-edge vortex formation for highly swept, sharp leading-edge lifting surface in supersonic flow.[9–12] Although the exact numerical mechanism by which Euler solvers produce a leading-edge vortex (which in reality are created by viscous forces) is not clearly understood, the significantly reduced computational resources required for solution of the Euler equations compared to those required for the Navier-Stokes equations make the Euler solvers attractive for studies involving sharp leading-edge lifting surfaces. Therefore, a Euler method, GEM3D,[14] was used for this study. Computations were performed for a forebody-strake configuration and compared to experimental data. These data include surface pressure, longitudinal force, and moment, and flow-visualization data for $M = 1.8$; a less extensive comparison is made for $M = 1.6$ and 2.0.

Model Description and Test Conditions

The wind-tunnel model consisted of a forebody 34.5 in. in length that would accommodate strakes. A photograph of the forebody-strake model installed in the NASA-Langley Unitary Plan Wind Tunnel[15] is presented in Fig. 1. The strake

Presented as Paper 89-0343 at the 27th Aerospace Sciences Meeting, Reno, NV, Jan. 9–12, 1989; received March 1, 1989; revision received June 11, 1992; accepted for publication June 18, 1992.

*Staff Engineer, Aerodynamics Department. Member AIAA.
†Assistant Head, Aerothermal Loads Branch, Structural Mechanics Division. Associate Fellow AIAA.

leading edges were machined as sharp as practical for aluminum which resulted in leading-edge radii of 0.003–0.005 in. The configuration was tested at a constant Reynolds number of 2 million/ft at Mach numbers of 1.60, 1.80, and 2.00. The angle of attack was varied from approximately 0–14 deg for a sideslip angle of 0 deg. Strips of transition-producing sand grit were placed 1.2-in. behind the nose of the model and 0.4-in. aft of the strake leading edge in the streamwise direction to ensure fully turbulent boundary-layer flow over most of the model surface, according to guidelines suggested in Ref. 16.

Euler Computational Method

General Discussion

The method applied in the present investigation uses a node-centered, hybrid finite-volume, central difference scheme with explicit artificial viscosity. It is tailored to supersonic free-stream flows and uses implicit marching based on a technique developed for an earlier full-potential method.[17] The method uses a spherical coordinate system and marches in the radial direction. Figure 2 shows the coordinate system together with the numerical representation of the forebody with flat strake. Also displayed in Fig. 2 are typical radial cuts showing spherical sectors and grids on which the crossflow computations are performed. Figure 3 shows views of typical grids at streamwise locations of 15- and 30-in. aft of the forebody apex. At a fixed radial cut, the unsteady Euler equation for the crossflow is solved by using a multistage Runge-Kutta integration with local time-stepping to accelerate convergence to a steady state. A combination of second-order and fourth-order artificial dissipation terms are added for stability and shock capturing. The fourth-order terms are to prevent odd and even node decoupling, whereas the second-order damping mainly smooths oscillations in regions of severe pressure gradients.

A converged solution is obtained when the value of the maximum flowfield residual is reduced below 0.01 on each solution plane. Numerical experiments showed that reducing the maximum residual by another factor of 10 did not change the computed surface pressures. Generally, reducing the maximum residual below 0.01 yielded an average flowfield residual an order of magnitude smaller.

Governing Equations

The Euler equation formulation presented here is relatively standard except for being expressed in a spherical coordinate system, and it is similar to the formulation of Ref. 14, where further details are available. In a Cartesian coordinate system, the differential form of the unsteady Euler equations are

$$\frac{\partial \boldsymbol{Q}}{\partial t} + \frac{\partial f}{\partial x} + \frac{\partial g}{\partial y} + \frac{\partial h}{\partial z} = 0 \tag{1}$$

where

$$\boldsymbol{Q} = (\rho, \rho u, \rho v, \rho w, E)^T \tag{2a}$$

$$f = (\rho u, p + \rho u^2, \rho uv, \rho uw, \rho uH)^T \tag{2b}$$

$$g = (\rho v, \rho uv, p + \rho v^2, \rho uw, \rho vH)^T \tag{2c}$$

$$h = (\rho w, \rho uw, \rho vw, p + \rho w^2, \rho wH)^T \tag{2d}$$

The total internal energy and total enthalpy are related to the flow variables by the following expressions:

$$E = [p/(\gamma + 1)] + \tfrac{1}{2}\rho(u^2 + v^2 + w^2) \tag{3}$$

$$H = [(E + p)/\rho] \tag{4}$$

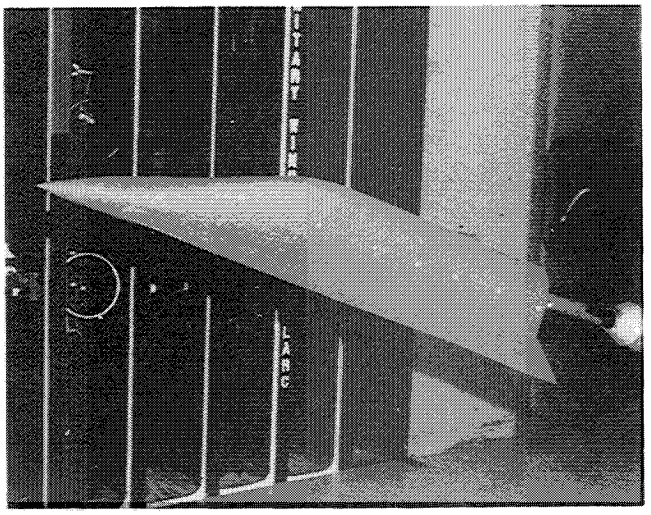

Fig. 1 Photograph of forebody-strake model installed in NASA Langley Unitary Plan Wind Tunnel.

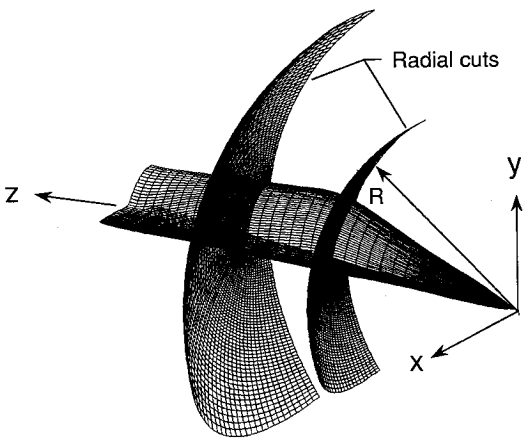

Fig. 2 Coordinate system showing typical spherical grids and numerical representation of forebody-strake.

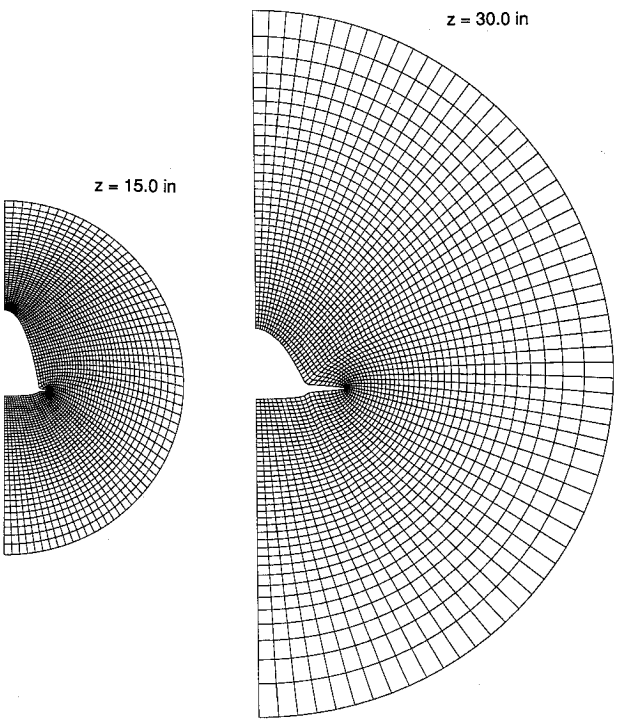

Fig. 3 Typical crossflow grids at selected streamwise stations.

Equations (1–4) are expressed in a spherical coordinate system by defining

$$\bar{x} = x/z \tag{5a}$$

$$\bar{y} = y/z \tag{5b}$$

$$R^2 = x^2 + y^2 + z^2 \tag{5c}$$

$$\bar{u} = u - \bar{x}w \tag{6a}$$

$$\bar{v} = v - \bar{y}w \tag{6b}$$

$$\bar{w} = \bar{x}u + \bar{y}v + w \tag{6c}$$

The Euler equations defined by Eq. (1) transform to

$$\frac{\partial \boldsymbol{Q}}{\partial t} + \frac{\Omega}{R}\left(\frac{\partial \bar{f}}{\partial \bar{x}} + \frac{\partial \bar{g}}{\partial \bar{y}} + 2\bar{I}\right) + \frac{1}{\Omega}\frac{\partial \bar{h}}{\partial R} = 0 \tag{7}$$

where

$$\Omega^2 = 1 + \bar{x}^2 + \bar{y}^2 \tag{8a}$$

$$\bar{f} = (\rho\bar{u},\ \rho u\bar{u} + p,\ \rho v\bar{u},\ \rho w\bar{u} - \bar{x}p,\ \rho H\bar{u})^T \tag{8b}$$

$$\bar{g} = (\rho\bar{v},\ \rho u\bar{v},\ \rho v\bar{v} + p,\ \rho w\bar{v} - \bar{y}p,\ \rho H\bar{v})^T \tag{8c}$$

$$\bar{h} = (\rho\bar{w},\ \rho u\bar{w} + \bar{x}p,\ \rho v\bar{w} + \bar{y}p,\ \rho w\bar{w} + p,\ \rho H\bar{w})^T \tag{8d}$$

$$\bar{I} = (\rho w,\ \rho uw,\ \rho vw,\ \rho w^2 + p,\ \rho Hw)^T \tag{8e}$$

Effect of Crossflow Grid Density

Previous work[18] for highly swept wings having rounded leading edges has indicated that grid density can affect the type of flow, i.e., separated or attached, computed by an Euler solver. Those results indicated that a leading-edge vortex formed for certain grid densities, but an attached-flow solution was obtained for higher grid densities. For the present investigation, the grid-density study focused on the α = 7.6-deg case because this angle of attack was the lowest at which experimental evidence of leading-edge separation was observed on the strake. It is reasoned that the sensitivity of the flow pattern to grid density would be greatest at this condition.

The effect of crossflow grid density on the resolution of the computed flowfields was investigated at a fixed Mach number and angle of attack for seven different crossflow grid densities at a constant marching stepsize of 0.5 in. Representative results are presented in Figs. 4, 5, and 6. For a grid density expressed as $I \times J$, I represents the number of points in a direction around the body and J represents the number of points from the body to the outer edge of the computation domain. The spacings are such that points are clustered near the strake leading edge in the I direction and near the body surface in the J direction.

Figure 4 shows isobars and entropy contours in the flowfield for a spanwise cut at z = 15.0 in. The isobar plots reveal nearly identical patterns for the entire flowfield when comparing the 61 × 57 and the 85 × 57 grids. The isobar pattern differs slightly for the 31 × 29 grid with the most noticeable difference being the smearing of the bow shock. The isobar patterns reveal no significant differences in the character of the flowfield as computed on all three grids.

Entropy gradients are directly related to fluid vorticity through integrated forms of the Euler equation such as Crocco's theorem.[19] The entropy contours of Fig. 4 may, therefore, be taken as indicators of vorticity in the vicinity of the strake leading edge. This interpretation of entropy contours is confirmed by velocity-vector plots and will be used subsequently in this article. Considering the entropy-contour plots

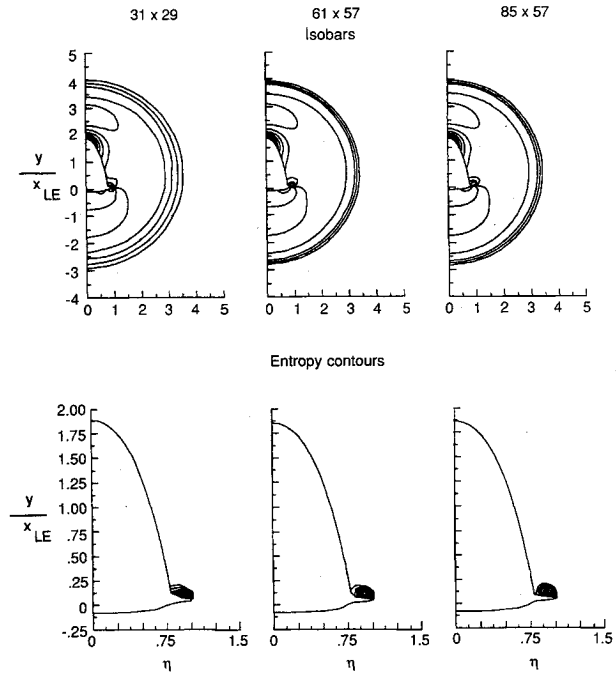

Fig. 4 Comparison of computed flowfield with variation in crossflow grid density (M = 1.8, α = 7.6 deg, z = 15 in.).

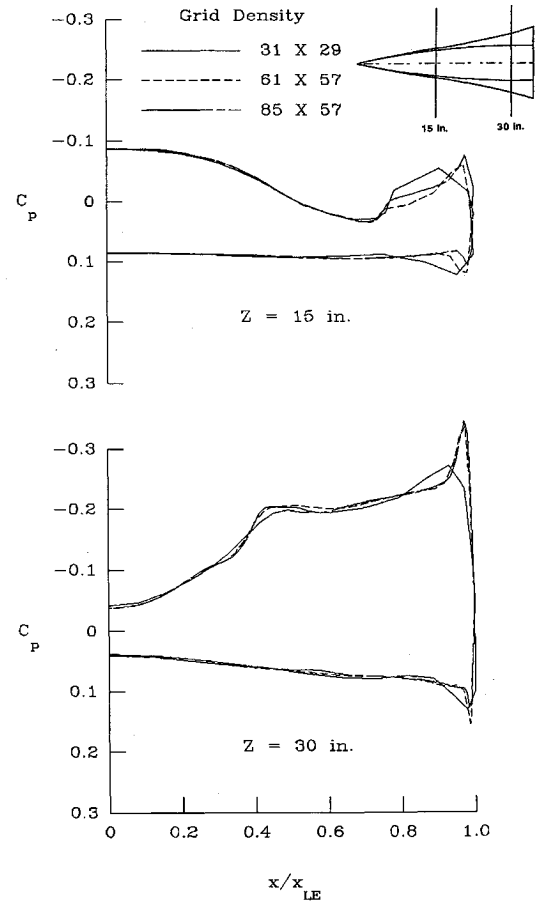

Fig. 5 Comparison of computed surface pressures with variation crossflow grid density (M = 1.8, α = 7.6 deg).

of Fig. 4, it is seen that a leading-edge vortex is predicted for every grid density shown, with the contour patterns being very nearly the same for the 61 × 57 and 85 × 57 grids. The existence or nonexistence of a predicted leading-edge vortex is insensitive to the crossflow-plane grid density, provided the

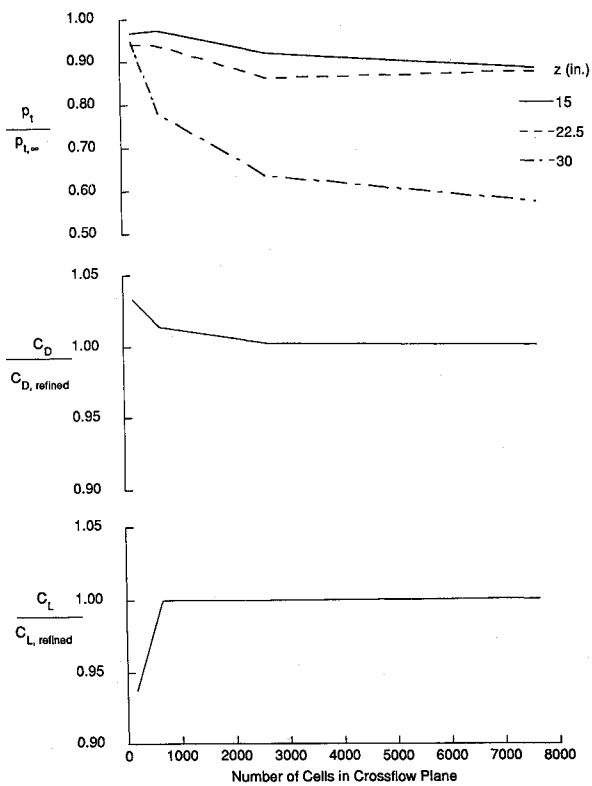

Fig. 6 Comparison of vortex total pressure and integrated quantitites with variation in crossflow grid density (M = 1.8, α = 7.6 deg).

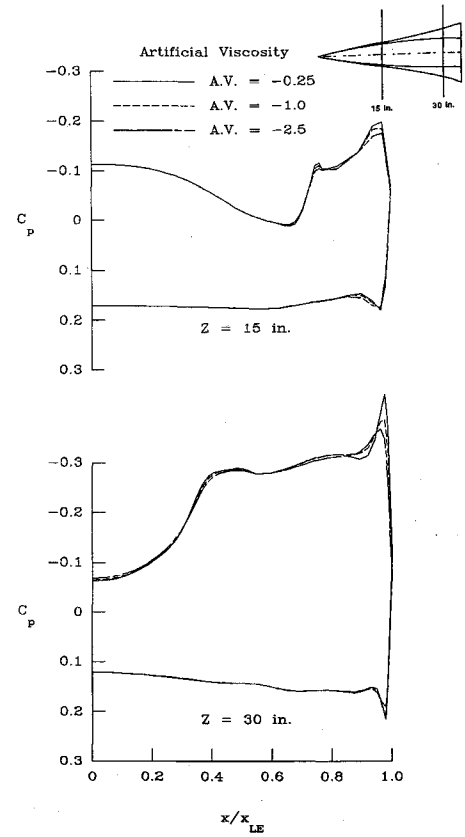

Fig. 7 Comparison of computed surface pressures with variation in second-order artificial viscosity (M = 1.8, α = 7.6 deg).

grid is dense enough to resolve the flowfield accurately in the first place. These results for a sharp leading-edge contrast with the Euler computations presented in Ref. 18 which treated wings having rounded leading edges.

Figure 5 shows computed spanwise surface-pressure distributions for grid densities of 31 × 29, 61 × 57, and 85 × 57 grid points at M = 1.8 and α = 7.6 deg. From the figure it is clear that the computed results are nearly identical for all three grid densities, except in the vicinity of the leading edge. The 31 × 29 grid results differ slightly from that of the 61 × 57 and 85 × 57 grids near the leading edge, but the 61 × 57 and 85 × 57 grid predictions are essentially identical.

Figure 6 shows the behavior of computed lift, drag, and minimum total pressure in the vortex as the grid density is varied over a wide range. The figure of merit for the grid-density study is taken as the number of computational cells in the crossflow plane, computed as $(I - 1) \times (J - 1)$. The aspect ratio of the cells was maintained at a value on the order of unity. The results shown indicate that when the number of cells exceeds a value ~3000, the indicated quantities are relatively insensitive to further refinements in grid density. Note that a 61 × 57 grid contains 3360 cells in the crossflow plane.

Based on the flowfield resolution shown in Fig. 4, the pressure distributions shown in Fig. 5, and the lift, drag, and total-pressure losses shown in Fig. 6, the 61 × 57 grid was considered sufficient, and was used for the computations presented in the remainder of this article.

Effect of Artificial Viscosity

The exact mechanism by which computational solutions of the Euler equations result in separation and vortices is not clearly understood. Strong transient shocks and/or artificial viscosity have been suggested as mechanisms.[20-22] It is important, therefore, to become aware of possible spurious effects or lack of consistency when applying Euler computations under conditions likely to involve separated flow. The effect of artificial viscosity on leading-edge vortex solutions of the Euler equations for conical delta wings has been examined by several investigators.[9-12,21-23] For delta wings having sharp leading edges, the solutions are relatively insensitive to variations in artificial viscosity. Configurations with wing-body combinations having sharp leading edges have also been investigated,[24] but the influence of artificial viscosity on Euler solutions involving three-dimensional vortical flows has not been extensively studied.

Table 1 Total-pressure loss in vortices for variation in second-order artificial damping (M = 1.8, α = 13.6 deg)

	Maximum total pressure loss in vortex, %		
z, in.	$A.V. = -0.25$	$A.V. = -1.0$	$A.V. = -2.5$
15	22.6	22.7	23.4
30	46.5	52.0	49.6

The effect of artificial viscosity was investigated by obtaining solutions for the uncambered strake at a fixed Mach number and angle of attack for independent variation in the second-order and fourth-order artificial viscosity coefficients. As discussed in Ref. 14, the fourth-order artificial viscosity is a background dissipation applied to the entire flowfield to prevent even/odd node decoupling, whereas the second-order artificial viscosity is weighted to provide dissipation in regions of large pressure gradients. It would therefore be expected that for phenomena in the vicinity of the strake leading edge, where gradients are large, variations in the fourth-order artificial viscosity would have very little effect. Computations in which the fourth-order artificial viscosity parameter was varied over a wide range confirmed this view. For this reason, only results showing the effects of varying the second-order artificial viscosity parameter are presented.

Figure 7 shows computed surface-pressure distributions at stations z = 15 in. and z = 30 in. for M = 1.8 and α = 13.6 deg. Pressures are presented for artificial viscosity ($A.V.$) coefficients of −0.25, −1.0, and −2.5. It is seen that all three pressure distributions agree except in a small region near the upper surface of the leading edge, where there are

slight differences. In this region, the solution corresponding to $A.V. = -2.5$ indicates a discernible suction peak. The solution corresponding to $A.V. = -1.0$ shows less of a suction peak, and the solution corresponding to $A.V. = -0.25$ a still smaller suction peak.

The predicted total-pressure losses due to the vortices for the indicated values of second-order artificial viscosity are given in Table 1. From the table, it is seen that these losses are relatively insensitive to the different values of artificial viscosity. Based on the results presented in Fig. 7 and in Table 1, it is seen that values of $A.V.$ in the range -0.25 to -2.5 should produce consistent solutions for the forebody strake. A value of $A.V. = -0.25$ is recommended in Ref. 25, and this value was used for the computations presented in the remainder of this article.

Comparison with Experiment

Effect of Angle of Attack

Euler code predictions and wind-tunnel data at a Mach number of 1.8 are presented in Figs. 8–11. Surface pressures, entropy contours, crossflow velocity vectors, and vapor-screen photographs are shown in Figs. 8 and 9 for angles of attack of 7.6 and 13.6 deg, respectively, for two different streamwise stations. Figure 10 is a planform oil-flow photograph and Fig. 11 presents computed and measured surface-pressure distributions along the configuration upper and lower center lines.

Figure 8a shows results for $\alpha = 7.6$ deg and $z = 15$ in., and Fig. 8b for $\alpha = 7.6$ deg and $z = 30$ in. As discussed previously, the leading-edge vortex is relatively weak at this angle of attack and provides a sensitive test of the Euler

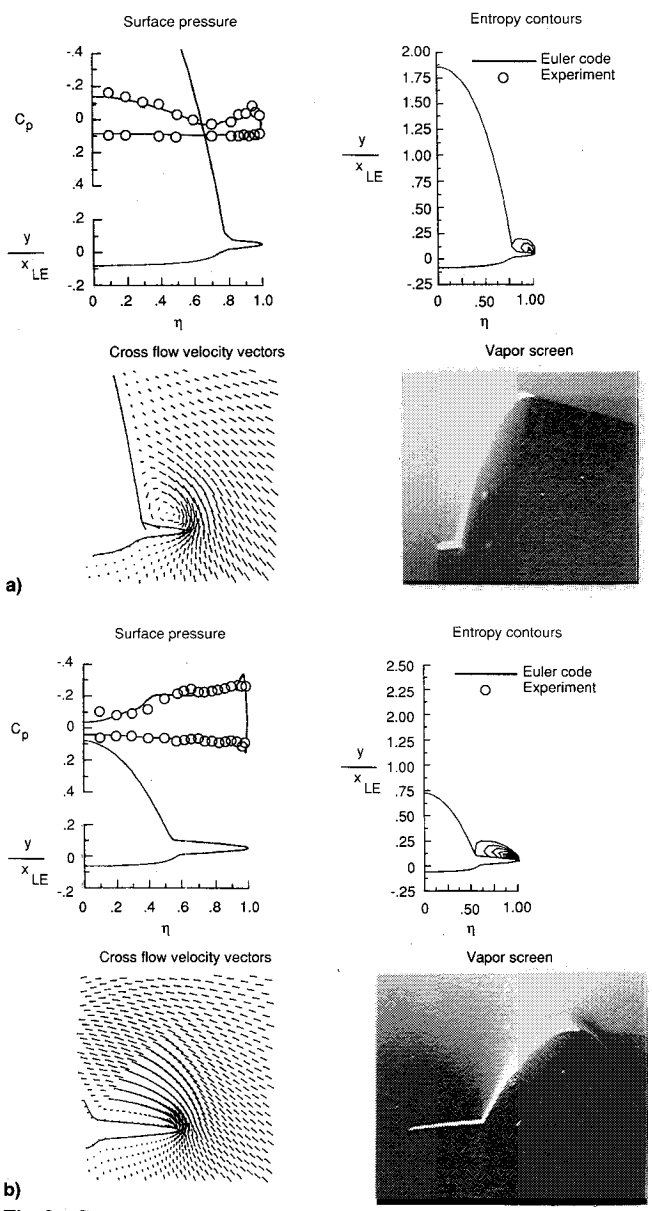

Fig. 8 Comparison of computed surface pressure and flowfield quantities with wind-tunnel observations: a) $M = 1.8$, $\alpha = 7.6$ deg, $z = 15$ in. and b) $M = 1.8$, $\alpha = 7.6$ deg, $z = 30$ in.

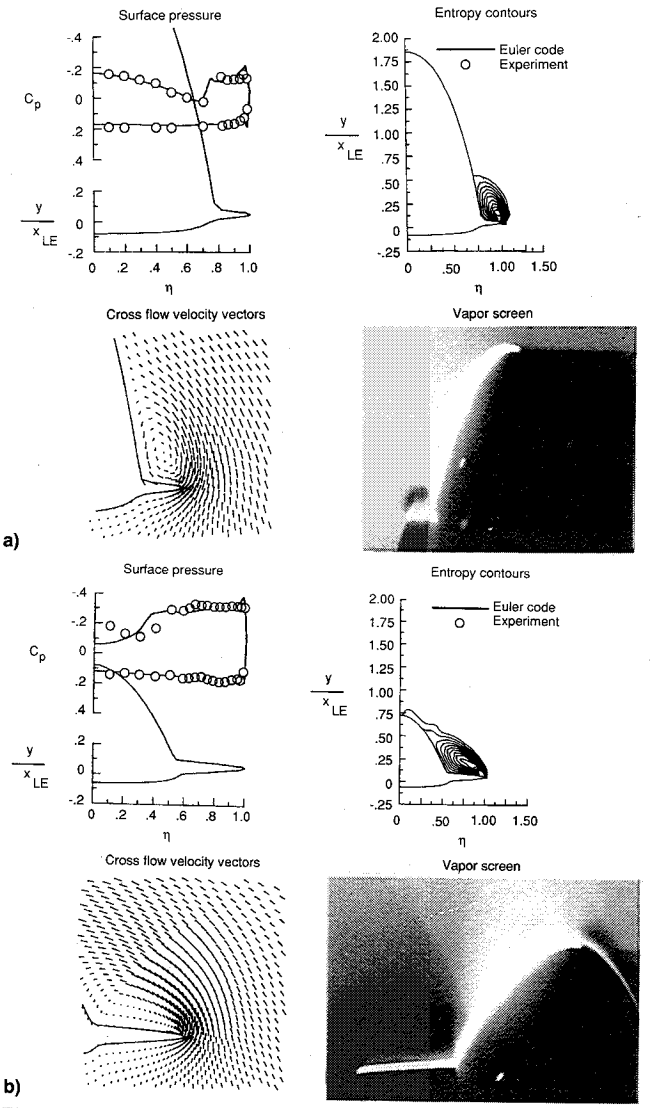

Fig. 9 Comparison of computed surface pressure and flowfield quantities with wind-tunnel observations: a) $M = 1.8$, $\alpha = 13.6$ deg, $z = 15$ in. and b) $M = 1.8$, $\alpha = 13.6$ deg, $z = 30$ in.

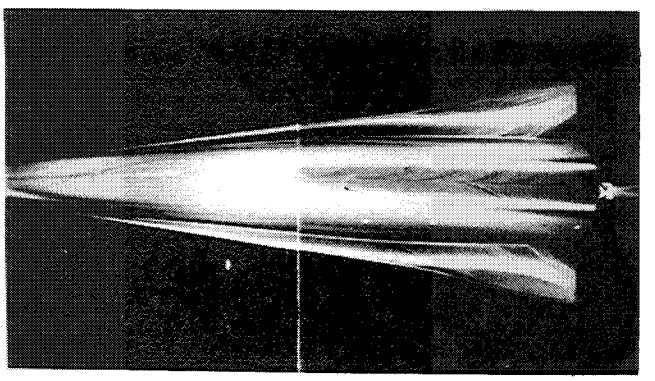

Fig. 10 Planform view of model with oil-flow patterns ($M = 1.8$, $\alpha = 10$ deg).

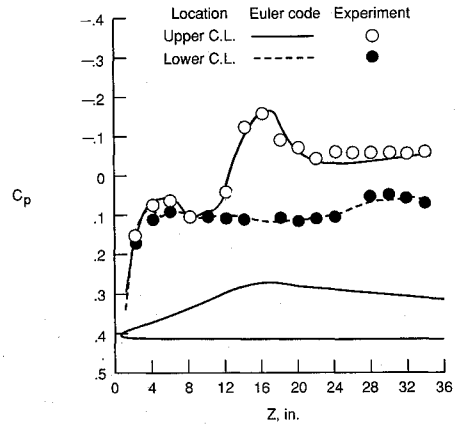

Fig. 11 Streamwise surface-pressure distributions on upper and lower centerlines (M = 1.8, α = 10 deg).

method's ability to predict the vortex. Considering the spanwise surface-pressure distribution in Fig. 8a, it is seen that the Euler predictions are in good agreement with the measured values on the entire surface at this station. The entropy contours and crossflow velocity vectors in Fig. 8a offer a clear computational prediction of a vortex emanating from the sharp leading edge of the strake. The spanwise surface-pressure distribution, both predicted and measured, is also consistent with there being a vortex at the leading edge of the strake. The predicted maximum total-pressure loss for the vortex at these conditions is approximately 10%, indicating a very weak vortex. However, the vapor-screen photograph, a relatively insensitive technique, does not reveal any indication of a vortex.

Figure 8b, which presents results for z = 30 in., shows good general agreement between the measured and computed surface pressures except on the upper surface inboard of η = 0.5. The reason for this is evidently due to a pair of shock-induced body vortices not predicted by the Euler code. The vapor-screen photograph suggests separated flow on the forebody near the upper centerline. These body vortices will be discussed in more detail later in this article when Figs. 10 and 11 are examined. The entropy contours again show a predicted leading-edge separation which is flattened and spread over most of the strake upper surface, and is either a vortex or separation bubble. For this station at z = 30 in., the vapor screen also shows faint but unmistakable evidence of a vortex or separation bubble on the strake upper surface emanating from the leading edge. In this figure, a computed embedded shock can be detected in the vector field as a line of discontinuities in the flow over the upper surface, although the vapor-screen evidence for an embedded shock is not definitive. The indicated shock is evidently curved, is of varying strength, and terminates somewhere in the flowfield. The foot of the shock appears above the separation bubble, and therefore, is not expected to influence the surface-pressure distribution. The recompression on the body upper surface is indicative of the attachment line of the leading-edge vortex. The maximum computed total-pressure loss in the vortex at this station is approximately 39% indicating that the leading-edge vortex increases in strength with respect to increasing streamwise station.

Figure 9 presents wind-tunnel observations and Euler computations at a higher angle of attack, α = 13.6 deg, which was the highest angle of attack in the experiment. The station at z = 15 in., Fig. 9a, shows clear evidence of a leading-edge vortex both experimentally and computationally. This is displayed in the computations by the rotationality of the crossflow velocity-vector field as well as the pattern of the entropy contours. In the vapor screen, the vortex feeding from the strake leading edge is clearly shown. The upper-surface pressure distribution, both experimental and computational, shows an expansion around the strake leading edge to a suction plateau. Inboard of the suction plateau is a strong recompression above the strake-body intersection followed by a mild re-expansion as the flow accelerates over the upper-body surface. The suction plateau terminating in a strong recompression on the body side is consistent with vortical flow, wherein the point of maximum recompression indicates an attachment or crossflow stagnation line. This interpretation closely parallels the predicted crossflow velocity-vector pattern. The maximum computed total-pressure loss in the vortex at this station and angle of attack is 23%, which is double the loss at the corresponding station for α = 7.6 deg.

The information displayed in Fig. 9b for station z = 30 in. also shows evidence of a leading-edge vortex together with additional complex flow phenomena. The computational prediction of a leading-edge vortex extending over the entire strake is indicated by the entropy contours and the crossflow velocity-vector patterns. In the entropy-contour plot, the closed-loop contours relate to the leading-edge vortex. The predicted maximum total pressure loss in the vortex at these conditions is approximately 52%. As mentioned earlier, the corresponding station for α = 7.6 deg had a predicted loss of 39%, indicating that the vortex is strengthened at the higher angle of attack α = 13.6 deg. In addition to closed-loop entropy contours, there is significant entropy indicated beyond the vortex and extending up the side of the body. The crossflow velocity-vector plot shows an embedded shock above the vortex similar to the corresponding station for α = 7.6 deg. Furthermore, this shock is clearly shown in the vapor-screen photograph. The predicted surface pressures are in good agreement on the entire lower surface, around the strake leading edge and on the upper surface except inboard from about η = 0.5. This difference is attributed to the vortices on the upper-body surface that are not predicted by the Euler solver.

Vortices on Upper Surface of Body

A pair of vortices over the top of the body near the upper centerline is visible in the vapor-screen photographs of Figs. 8b and 9b. Figure 10 presents additional evidence of this flow feature using a planform view of the model with oil-flow patterns at M = 1.8 and $\alpha \approx$ 10 deg. The 10-deg angle of attack was the highest value at which oil-flow patterns could be recorded, but a comparison of vapor-screen photographs at $\alpha \approx$ 10 deg and $\alpha \approx$ 14 deg showed identical flow structure for these two angles of attack. Therefore, the oil-flow data at $\alpha \approx$ 10 deg are representative of the $\alpha \approx$ 14-deg flowfield.

It is seen from Fig. 10, that there is a characteristic "herringbone" pattern in the oil-flow data in the region of the upper surface centerline. This pattern is indicative of a pair of vortices in the flow above the body, with a reattachment line on the upper centerline. This pattern originates just aft of the canopy.

A possible cause for the vortex pair can be inferred from the results given in Fig. 11, which presents experimental and computational surface streamwise pressure distributions on the upper and lower centerlines of the body. The results are given for the same conditions as the oil flows in Fig. 10, namely for M = 1.8 and $\alpha \approx$ 10 deg. The upper-surface pressure distribution reveals an expansion over the canopy, followed by a shock after which the surface pressure is nearly constant. Allowing the fairly coarse streamwise resolution in the computed pressures of 72 points over the length of the configuration, it is seen that the computed values agree well with the experimental values except on the upper surface aft of the recompression. According to the work presented in Refs. 26–28, a three-dimensional surface shock having a 50% or higher static-pressure rise will tend to separate a turbulent boundary layer. The predicted as well as the measured pressures shown in Fig. 11 achieve this criterion which supports the hypothesis of the separation being shock-induced. It should be observed that there is no evidence of these upperbody vortices being

predicted by the Euler code. This is expected, since the phenomena shown in Figs. 10 and 11 represent a complex interaction between the shock and the boundary layer that is beyond the scope of an inviscid theory.

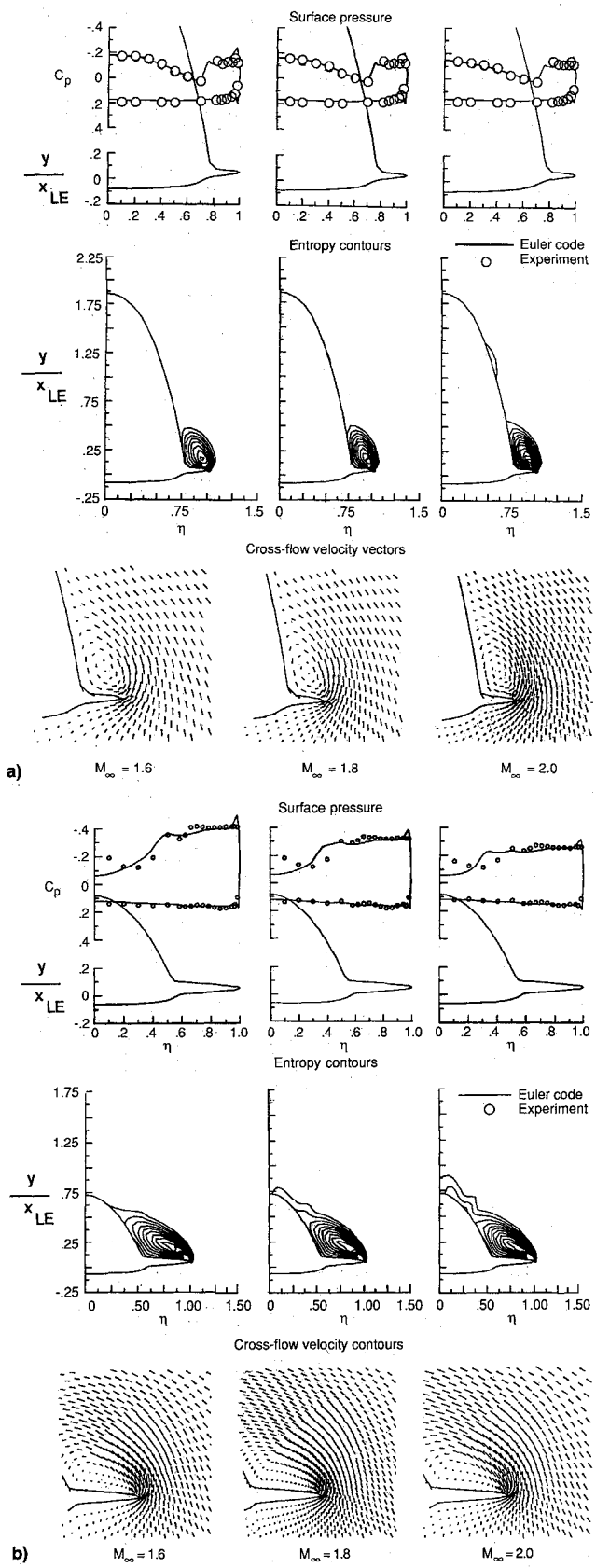

Fig. 12 Surface-pressure and flow quantities with variation in freestream Mach number: a) α = 14 deg, z = 15 in. and b) α = 14 deg, z = 30 in.

Effect of Variation in Mach Number

Figure 12 shows computed flowfield quantities and both computed and measured surface pressures at $\alpha \approx 14$ deg, z = 15, and 30 in. for M = 1.6, 1.8, and 2.0. Considering the streamwise station at z = 15 in. (Fig. 12a), it is seen that there is general similarity in the flows as Mach number increases. The agreement between computed and measured surface pressures is good across the Mach number range. The predicted pressure distribution shows a significant suction peak on the upper surface of the strake leading edge at M = 1.6. The magnitude of this peak decreases at the higher Mach numbers. The entropy contours and crossflow velocity vectors show a computed leading-edge vortex that changes shape slightly as the Mach number increases. There appears to be a strengthening of the vortex as Mach number is increased as evidenced by the maximum total-pressure loss shown in Table 2. Figure 12b presents results for station z = 30 in. Considering first the spanwise surface pressures, it is seen that the values on the lower surface, both computed and measured, differ very little as the freestream Mach number varies. By contrast, the suction C_p on the upper surface decreases with increasing Mach number for both the computed and measured distributions. As was true for previously discussed results, the computed and measured surface-pressure distributions agree quite well except on the upper part of the body surface near the previously mentioned shock-induced separation on the upper body. The crossflow velocity-vector plots give a clear indication of a curved embedded shock above the vortex for each of the Mach number cases shown.

Integrated Results

Figure 13 presents computed and measured force and moment characteristics at M = 1.8. The computed results are obtained by numerical integration of the surface pressures predicted by the Euler code. The drag coefficient includes both the inviscid and skin-friction contributions. The skin-friction drag coefficient was a constant value of 0.0071 obtained by the method discussed in Ref. 29. The results presented in Fig. 13 show excellent agreement between computed and measured values for both lift and drag over the range of α considered. The pitching moment shows good agreement between computation and measurement except at the lower angles of attack where the pitching moment is underpredicted. The integrated results were found to be relatively insensitive to crossflow grid density, in that the results for the 31 × 39 grid were nearly the same as for the 61 × 57 and 85 × 57

Table 2 Comparison of computed total-pressure loss in vortices for variation in freestream Mach number (61 × 57, α = 13.6 deg)

	Maximum total pressure loss in vortex, %		
z, in.	M = 1.6	M = 1.8	M = 2.0
15	20	23	26
30	48	52	59

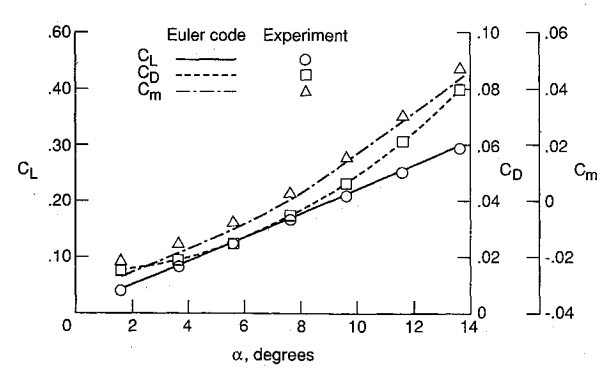

Fig. 13 Comparison of computed and measured force and moment, M = 1.8.

grids. These results suggest the preliminary design can be done successfully on the more economical coarse grid.

Summary and Conclusions

Euler flowfield computations for a fighter-type forebody with a sharp leading-edge, uncambered strake have been performed and compared to wind-tunnel data. Extensive comparisons were presented for a freestream Mach number of 1.8 and $\alpha = 7.6$ and 13.6 deg, with selected results at $M = 1.6$ and $M = 2.0$ for Mach number effects at the high angle-of-attack case. The effect of crossflow-plane grid density, artificial viscosity, angle of attack, and streamwise station on the flowfield were examined. Crossflow velocity vectors, entropy contours, vapor screens, surface pressures, and oil flows were presented and analyzed. Emphasis was placed on the prediction and characteristics of leading-edge vortices and embedded shocks. Longitudinal forces and moments were computed and compared with measured values.

It was shown that increasing the crossflow-plane grid density resulted in a better resolution of the flowfield details, but the general characteristics of the flowfield remained the same, provided a threshold of approximately 3000 crossflow grid cells was exceeded. The surface pressures and total forces and moments were relatively insensitive to the variation in crossflow grid density. The flowfield details, surface pressures, and integrated results were generally insensitive to large variations in the artificial viscosity. The strength of leading-edge vortices generally increased with increasing angle of attack, increasing streamwise station, and increasing freestream Mach number.

It was found that the inviscid flowfield, including vortices feeding from a strake with a sharp leading edge and an embedded shock originating aft of the canopy, was predicted with good fidelity to the experimentally observed flow characteristics. Embedded shock-induced separation resulting in vortices above the body were not predicted. This indicates that viscosity plays a dominant role in the formation of these shock-induced vortices. It was found that the features of the computed flowfield could be understood and compared to vapor-screen observations using a combination of entropy contours and crossflow velocity vectors.

The computed spanwise surface-pressure distributions were found to agree well with the measured values except for the upper surface of the body aft of the canopy region in the vicinity of the top centerline. This is the region covered by the shock-induced vortices. The surface-pressure agreement was consistent for angle-of-attack variations from 0 to 14 deg, and for freestream Mach numbers in the range 1.6–2.0

References

[1]Nielsen, J. N., "Nonlinearities in Missile Aerodynamics," AIAA Paper 78-20, Jan. 1978.

[2]McCroskey, W. J. (ed.), "High Angle-of-Attack Aerodynamics," AGARD CP-247, Jan. 1979.

[3]Peake, D. J., and Tobak, M., "Three-Dimensional Interactions and Vortical Flows with Emphasis on High Speeds," AGARD AG-252, July 1980.

[4]Wendt, J. F. (ed.), "High Angle-of-Attack Aerodynamics," AGARD LS-121, Dec. 1982.

[5]Young, A. D. (ed.), "Aerodynamics of Vortical Type Flows in Three Dimensions," AGARD CP-342, July 1983.

[6]Campbell, J. F., Osborn, R. F., and Foughner, J. T. (eds.), "Vortex Flow Aerodynamics," Vol. 1, NASA CP-2416, Vol. 2, NASA CP-2417, Oct. 1985.

[7]Granger, R. A., and Wendt, J. F., "Introduction to Vortex Dynamics," von Karman Inst. for Fluid Dynamics Lecture Series 1986-08, Rhode-Saint-Genese, Belgium, May 1986.

[8]Salas, M. D. (ed.), *Studies of Vortex Dominated Flows*, Springer-Verlag, New York, Nov. 1986.

[9]Newsome, R. W., and Kandil, O. A., "Vortical Flow Aerodynamics—Physical Aspects and Numerical Simulation," AIAA Paper 87-0205, Jan. 1987.

[10]Murman, E. M., and Miller, D. S., "Comparison of Computations and Experimental Data for Leading Edge Vortices—Effects of Yaw and Vortex Flaps," AIAA Paper 86-0439, Jan. 1986.

[11]Powell, K., Murman, E., Perez, E., and Baron, J., "Total Pressure Loss in Vortical Solutions of the Conical Euler Equations," AIAA Paper 85-1701, July 1985.

[12]Murman, E. M., Powell, K. G., Goodsell, A. M., and Landahl, M., "Leading-Edge Vortex Solutions with Large Total Pressure Losses," AIAA Paper 87-0039, Jan. 1987.

[13]Pittman, J. L., Bonhaus, D. L., and Siclari, M. J., "Strake Camber and Thickness Design Procedure for Low Alpha Supersonic Flow," *Journal of Aircraft*, Vol. 27, No. 6, 1990, pp. 481–487.

[14]Siclari, M. J., and Del Guidice, P., "A Hybrid Finite Volume Approach to Euler Solutions for Supersonic Flows," AIAA Paper 88-0225, Jan. 1988.

[15]Jackson, C. M., Jr., Corlett, W. A., and Monta, W. J., "Description and Calibration of the Langley Unitary Plan Wind Tunnel," NASA TP-1905, Nov. 1981.

[16]Braslow, A. L., and Knox, E. C., "Simplified Method for Determination of Critical Height of Distributed Roughness Particles for Boundary-Layer Transition at Mach Numbers from 0 to 5," NACA TN 4363, Sept. 1958.

[17]Siclari, M. J., "An Improved Version of NCOREL: A Computer Program for 3D Nonlinear Supersonic Potential Flow Computations," NASA CR-4165, July 1988.

[18]Newsome, R. W., "A Comparison of Euler and Navier-Stokes Solutions for Supersonic Flow over a Conical Delta Wing," AIAA Paper 85-0111, Jan. 1985.

[19]Anderson, J. D., Jr., "Modern Compressible Flow with Historical Perspective," McGraw-Hill, New York, 1982, pp. 165–167.

[20]Salas, M. D., "Recent Developments in Transonic Euler Flow over a Circular Cylinder," *Mathematics and Computers in Simulation*, Vol. 25, No. 3, 1983, pp. 232–236.

[21]Rizzi, A., "Damped Euler-Equation Method to Compute Transonic Flow Around Wing-Body Combinations," *AIAA Journal*, Vol. 20, No. 10, 1982, pp. 1321–1328.

[22]Fujii, K., "Evaluation of Euler and Navier-Stokes Solutions for Leading-Edge and Shock-Induced Separations," AIAA Paper 85-1563, July 1985.

[23]Kandil, O. A., "Influence of Numerical Dissipation in Computing Supersonic Vortex-Dominated Flows," AIAA Paper 86-1073, May 1986.

[24]Klopfer, G. H., and Nielsen, J. N., "Euler Solutions for Wings and Wing-Body Combination at Supersonic Speeds with Leading-Edge Separation," AIAA Paper 80-0126, Jan. 1980.

[25]Siclari, M. J., "GEM3D: An Euler Code for Supersonic/Hypersonic Aircraft," Grumman Corp., Rept. RE-766, Bethpage, New York, March 1989.

[26]Stanewsky, E., and Little, B. H., Jr., "Studies of Separation and Reattachment in Transonic Flow," AIAA Paper 70-541, April 1970.

[27]Korkegi, R. H., "A Simple Correlation for Incipient Turbulent Boundary-Layer Separation Due to a Skewed Shock Wave," *AIAA Journal*, Vol. 11, No. 11, 1973, pp. 1578, 1579.

[28]Rose, O. J., Miller, D. S., Pittman, J. L., Ashill, P. R., and Fulker, J. L., "Full-Potential Analysis of the Supersonic Delta Wing-Body," *Journal of Aircraft*, Vol. 20, No. 3, March 1989, pp. 235–240.

[29]Sommer, S. C., and Short, B. J., "Free-Flight Measurements of Turbulent-Boundary-Layer Skin Friction in the Presence of Severe Aerodynamic Heating at Mach Numbers from 2.8 to 7.0," NACA TN-3391, March 1955.